PHYSICAL REVIEW B VOLUME 57, NUMBER 10 1 MARCH 1998-II

Infrared activity in the Aurivillius layered ferroelectric $SrBi_2Ta_2O_9$

M. P. Moret* and R. Zallen
Department of Physics, Virginia Tech, Blacksburg, Virginia 24061

R. E. Newnham
Department of Materials Science and Engineering, Pennsylvania State University, University Park, Pennsylvania 16802

P. C. Joshi and S. B. Desu
Department of Materials Science and Engineering, Virginia Tech, Blacksburg, Virginia 24061

(Received 29 September 1997)

Experimental studies were carried out on infrared-active phonons in the Aurivillius ferroelectric $SrBi_2Ta_2O_9$ (SBT), using reflectivity measurements (down to $200\,cm^{-1}$) and transmission measurements (down to $100\,cm^{-1}$) on crystals, pellets, and thin films. An analysis was done of the contrasting consequences of the competing orthorhombic and pseudotetragonal symmetries in SBT. Reflectivity results for light polarized in the ab plane show that the anisotropy in this plane is small in the frequency range from 300 to $1200\,cm^{-1}$, indicating the influence of the approximate tetragonal symmetry. Dielectric dispersion properties were derived for this polarization ($E\perp c$) in this frequency range. The transverse-optical (TO) and longitudinal-optical (LO) frequencies corresponding to the dominant $E\perp c$ band are 613 and $773\,cm^{-1}$, respectively. This strong, high-frequency band arises from a mode dominated by the motion of the oxygen sublattice; its TO and LO frequencies yield an oxygen-ion Szigeti effective charge of $-1.5e$. Frequency estimates for the TO (LO) pairs of other strong bands are 188(330) and 334(451) cm^{-1} for $E\perp c$, and 610(675) and 780(815) cm^{-1} for $E\| c$. In addition to the main infrared bands, the main Raman bands of SBT are also reported. [S0163-1829(98)03010-0]

I. INTRODUCTION

Bengt Aurivillius reported on the structures of the mixed bismuth-oxide layer-structure compounds in 1949,[1] and the ferroelectric nature of the Aurivillius phases was discovered about a decade later.[2,3] In recent years, these materials have emerged as important candidates for nonvolatile ferroelectric memories.[4] A 256-kilobyte random-access memory has been reported by Araujo *et al.*,[5] using $SrBi_2Nb_xTa_{2-x}O_9$. $SrBi_2Ta_2O_9$ (strontium bismuth tantalate, SBT) is an important component of the thin-film ferroelectrics currently under development.

The crystal structure of SBT was investigated in 1973 by Newnham *et al.*[6] and in 1992 by Rae and co-workers.[7] The structure is orthorhombic, only slightly distorted from tetragonal. It consists of perovskitelike $(SrTa_2O_7)^{--}$ slabs alternating with $(Bi_2O_2)^{++}$ layers. The stacking axis (normal to the layers) is customarily defined as the c axis, with the a axis being the orthorhombic twofold symmetry axis (the polar-axis direction for ferroelectricity). In this $A2_1am$ space-group setting, the orthorhombic c axis coincides with the symmetry axis of the parent tetragonal structure ($I4/mmm$). The detailed structures obtained by Newnham *et al.*[6] and by Rae and co-workers[7] differ only slightly, and both yield a spontaneous a-axis polarization of roughly $10\,\mu C/cm^2$. The main contribution to the polarization arises from the off-center position of the Ta^{5+} ion relative to its octahedron of surrounding oxygens.[6]

In this paper, we present results of experimental studies of infrared-active lattice vibrations in $SrBi_2Ta_2O_9$. Raman-active modes in SBT have been reported for powder samples.[8] Infrared-active modes in SBT have, to our knowledge, not yet been investigated. Our study includes infrared measurements on both single crystals and polycrystalline films.

Experimental techniques are described in Sec. II. Section III presents a symmetry analysis of lattice vibrations in SBT, and compares the consequences of the orthorhombic crystal symmetry with those of the approximate tetragonal symmetry. X-ray-diffraction data on our samples is shown in Sec. IV. Section V presents our reflectivity results and discusses the infrared dielectric dispersion of SBT. The vibrational eigenvector and effective charges of the mode responsible for the main infrared band are analyzed in Sec. VI. Transmission measurements are presented in Sec. VII, which contains an inventory of the measured infrared-active phonon frequencies and also includes our measured Raman frequencies for SBT. A summary is given in Sec. VIII.

II. EXPERIMENT

Two main types of SBT samples were investigated, single crystals and polycrystalline films. The crystals were grown from the melt, using the method described in Ref. 6. Crystals were clear plates with dimensions typically about $2\times 2\times 0.1\,mm^3$. Their large surfaces were perpendicular to the crystal c axis. The domain orientation in the ab plane was random, since the crystals were not poled. The polycrystalline films were made by a metalorganic solution-deposition technique using, as precursors, strontium acetate, bismuth 2-ethylhexanoate, and tantalum ethoxide. The procedure is described in Ref. 9. The solution was spin coated onto a 0.3

mm-thick optical-quality silicon substrate and annealed at 650 °C for 30 min, yielding a well-crystallized film about 250 nm thick. Measurements were also made on a polycrystalline pressed pellet of SBT made by standard calcination techniques and sintered at 1100 °C for one hour, and on thin films made by pulsed laser deposition.[10]

The infrared measurements were carried out with a BOMEM DA-3 FTIR spectrometer. A pyroelectric detector was used to cover the wave number region from 100 to 700 cm^{-1}; a cooled HgCdTe detector was used from 500 to 2000 cm^{-1}. Spectra were collected with 4 cm^{-1} resolution, with 500 interferometer sweeps added for each spectrum. Reflectivity measurements were performed on the crystals and the pressed pellet; transmission measurements were made on the films.

Other experiments done on these samples include x-ray diffraction and Raman scattering. The x-ray measurements were made with a Scintag XDS-2000 diffractometer using Cu radiation at 1.54 Å. Raman measurements were made with a SPEX 1403 scanning spectrometer and a Dilor XY Raman microprobe.

III. SYMMETRY ANALYSIS OF LATTICE VIBRATIONS IN SBT

SBT is orthorhombic; the space group is $A2_1am$ (C_{2v}^{12}, number 36 in the standard listing). The dimensions of the rectangular parallelepiped unit cell are (in Å) $a=5.531$, $b=5.534$, $c=24.984$. This unit cell contains four $\mathrm{SrBi_2Ta_2O_9}$ formula units (56 atoms). The primitive cell, the smallest translational unit, is half as large, containing two formula units (28 atoms), since the $A2_1am$ unit cell is face centered on the A face and contains two lattice points. The $(\mathrm{SrTa_2O_7})^{--}$ perovskite slab, perpendicular to the c axis, is a double layer of corner-sharing $\mathrm{TaO_6}$ octahedra, with Sr atoms in the midplane. (There are many structural similarities between SBT and the bismuth-based ‘‘two-layer’’ cuprate superconductor $\mathrm{Bi_2Sr_2CaCu_2O_8}$.[11]).

Reasonably informative perspective diagrams of the complex crystal structure of SBT appear in the literature.[12,13] It should be noted that the unit cell indicated in those diagrams is invariably (in a practice dating back to Aurivillius[12]) not the orthorhombic unit cell but is instead the smaller pseudotetragonal unit cell (with dimensions, in Å, of $c=24.98$ and $a=b=3.91=5.53/\sqrt{2}$) that contains two formula units and corresponds to the approximate $I4/mmm$ (D_{4h}^{17}) symmetry. The tetragonal unit cell is body centered, containing two lattice points and hence two primitive cells. Thus the pseudotetragonal primitive cell contains only one formula unit (14 atoms). While the ‘‘approximate tetragonal symmetry’’ thus provides a nice simplification for visualizing and dealing with the complex SBT structure, the actual broken-symmetry aspect corresponding to the true orthorhombic symmetry is responsible for SBT’s ferroelectricity: the tetragonal structure allows no polar axis, the orthorhombic structure does. It is necessary to take cognizance of both symmetries that ‘‘coexist’’ in SBT.

In the tetragonal structure, all atoms lie on factor-group symmetry elements of $I4/mmm$.[14] The strontiums and the perovskite-slab midplane oxygens are invariant under all sixteen $I4/mmm$ symmetry operations.[14,15] In the orthorhombic structure, all atoms are in general positions of the $A2_1\,am$ space group[16] with the exception of the perovskite-midplane atoms (the strontiums and one-ninth of the oxygens).[17] Those atoms are on the perpendicular-to-c mirror plane (m of $A2_1am$), a symmetry element present in both $I4/mmm$ and $A2_1am$. Adjacent perovskite-midplane strontiums (or oxygens) are translationally equivalent in the tetragonal structure, translationally inequivalent in the orthorhombic. Adjacent perovskite slabs are translationally equivalent in both structures. Orthogonal in-the-slab directions (a and b) are equivalent by symmetry in the tetragonal structure; they are different (a is the polar axis) in the orthorhombic.

TABLE I. Number of infrared and Raman eigenfrequencies expected for tetragonal and orthorhombic SBT.

Optical experiment	Tetragonal	Orthorhombic
Infrared ($E\parallel c$)	6	19
Infrared ($E\perp c$)	7	42 (21 $E\parallel a$, 21 $E\parallel b$)
Raman (strongest, $aa+bb+cc$)	4	21
Raman (all)	12	81

The four factor-group operations of orthorhombic SBT are: 1, the identity; 2_a, the twofold screw axis parallel to the a axis; 2_b, the glide plane perpendicular to the b axis with glide direction along the a axis; and 2_c, the mirror plane perpendicular to the c axis (2_a, 2_b, and 2_c correspond, respectively, to 2_1, a, and m of $A2_1\,am$). The phonon symmetries correspond to the irreducible representations contained in Γ, the 84-dimensional representation generated by the displacements of the 28 atoms in one primitive cell.[18]

The decomposition of Γ yields

$$\Gamma=22A_1+20A_2+20B_1+22B_2. \tag{1}$$

Subtracting the three acoustic modes yields the symmetry types of the 81 zone-center optical modes of SBT:

$$\Gamma^{\mathrm{opt}}=21A_1+20A_2+19B_1+21B_2. \tag{2}$$

Since the A_1, B_1, and B_2 modes are infrared active (for $E\parallel a$, $E\parallel c$, and $E\parallel b$, respectively), 61 infrared frequencies are permitted. All 81 optical modes are Raman active.

For tetragonal SBT, the primitive-cell representation Γ is 42 dimensional and there are 10 irreducible representations for D_{4h} symmetry. The decomposition of Γ yields

$$\Gamma=4A_{1g}+2B_{1g}+6E_g+7A_{2u}+B_{2u}+8E_u. \tag{3}$$

Subtracting the three acoustic modes yields

$$\Gamma^{\mathrm{opt}}=4A_{1g}+2B_{1g}+6E_g+6A_{2u}+B_{2u}+7E_u. \tag{4}$$

Since the A_{2u} and E_u modes are infrared active, the tetragonal structure permits 13 infrared frequencies.

Table I summarizes the contrasting predictions, *vis-à-vis* optical experiments, for tetragonal and orthorhombic SBT. For light polarized in the ab plane ($E\perp c$), only 7 one-phonon infrared lines are permitted by the tetragonal structure, compared to 42 for the orthorhombic. The tetragonal structure is centrosymmetric, so that there is mutual exclusion between infrared and Raman activity. But for the orthorhombic structure, the infrared modes are also Raman active.

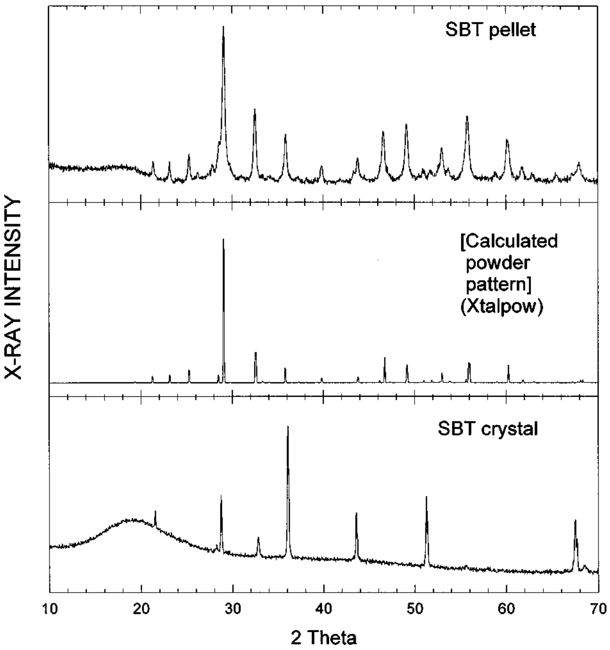

FIG. 1. X-ray-diffraction patterns of $SrBi_2Ta_2O_9$.

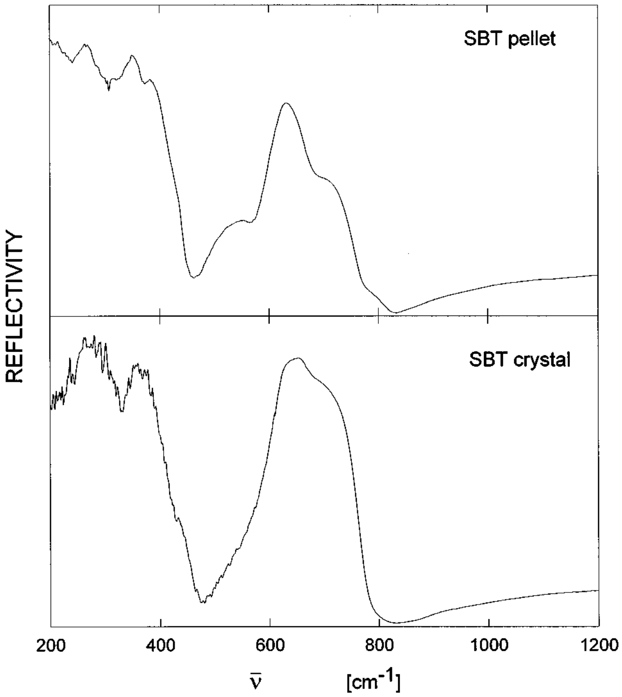

FIG. 2. Infrared reflectivity of polycrystalline and single-crystal SBT. The crystal-platelet surface is perpendicular to the c axis.

The third row in Table I corresponds to Raman lines having contributions from all the diagonal components: aa, bb, and cc. These dominant Raman lines arise from the fully symmetric modes: 4 A_{1g} modes for the tetragonal structure, 19 A_1 modes for the orthorhombic.

For the orthorhombic structure, with its low symmetry and 28-atom primitive cell, none of the optical-mode eigenvectors are symmetry-determined. This is true even for the tetragonal structure, with its higher symmetry (16 factor-group operations) and simpler (14-atom) primitive cell. Instructive pictures of some symmetrized coordinates for the tetragonal structure have been given by Graves *et al.*;[19] the actual vibrational eigenvectors are linear combinations of these.

IV. DIFFRACTION RESULTS

All of the samples studied were checked by x-ray diffraction to confirm that SBT was the predominant component. Results for a pressed pellet and a single crystal are shown in Fig. 1; results on the thin films are given in Ref. 9. The top and bottom panels of Fig. 1 show diffraction measurements taken in the usual Bragg-Brentano $\theta/2\theta$ configuration. The middle panel shows a calculated powder pattern based on the $A2_1\,am$ structure of SBT.[20]

The top two panels of Fig. 1 match very closely in both the positions and relative intensities of the diffraction peaks. This indicates that the pressed pellet closely approximates polycrystalline $SrBi_2Ta_2O_9$ with randomly oriented grains. The strongest peak in both diffraction patterns (near 29°) corresponds to the (1 1 5) line; the next strongest peak (near 32.5°) corresponds to (2 0 0) and (0 2 0).

All of the peaks observed in the measured single-crystal diffraction pattern, shown in the bottom panel of Fig. 1, are attributable to SBT. Fewer peaks appear here than for the polycrystalline pellet. The two lines (at 29° and 32.5°) that dominate the pellet pattern are still present, but the crystal pattern is dominated by a series of six lines (21.5°, 28.5°, 36°, 43.5°, 51°, 67.5°) that can all be indexed as $(h,k,l)=(0,0,l)$, with the observed lines corresponding to l values of (6, 8, 10, 12, 14, 18), respectively. These results indicate that the scattering vector (which, in these measurements, was normal to the large faces of the platelike crystal) is parallel to the crystal c axis, consistent with previous work[6] on the orientation of thin SBT crystals.

V. INFRARED REFLECTIVITY AND DIELECTRIC DISPERSION

Figure 2 presents results for the reflectivity of a polycrystalline pellet and a single crystal of SBT. The range covered is 200 to 1200 cm^{-1}. (The frequency or photon-energy scale used throughout this paper is in terms of the equivalent wave number units, $\nu=\lambda^{-1}$.) Unpolarized light was used, since the pellet was a composite of randomly oriented crystallites and the crystal was too small to allow adequate signal with the use of a polarizer. The pellet reflectivity includes contributions from all three polarizations, $E\|a$, $E\|b$, and $E\|c$. Because of the near-normal (11°) incidence used and the $\perp c$ orientation of the crystal platelet, the crystal reflectivity of Fig. 2 essentially includes contributions only from $E\|a$ and $E\|b$.

The crystal reflectivity exhibits a high-reflectivity phonon band (in old terminology, a reststrahlen band) extending approximately from 600 to 800 cm^{-1}. The low-frequency edge of this high-reflectivity plateau is associated with a strongly infrared-active transverse-optical (TO) mode; the high-frequency edge is associated with the corresponding longitudinal-optical (LO) mode. This 600–800 cm^{-1} TO-LO band is the dominant feature of the crystal spectrum. It is

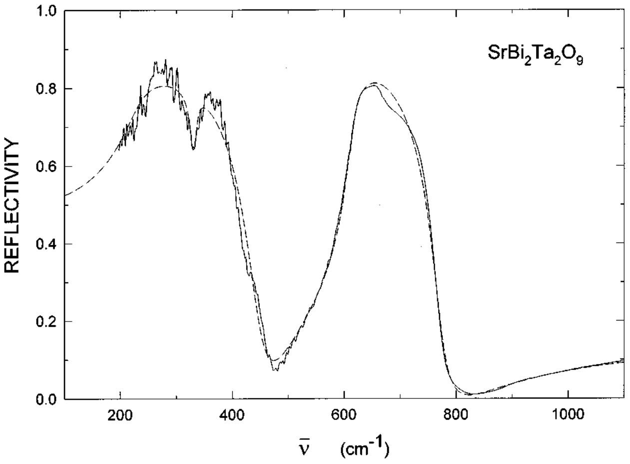

FIG. 3. Infrared reflectivity of crystalline SBT for $E \perp c$. The solid curve is the experimental data; the dashed curve is the theoretical fit described in the text.

also evident in the reflectivity of the polycrystalline pellet, as seen in the top panel of Fig. 2. In addition, other features appear in the pellet spectrum; notably the band at 540 cm^{-1}, the sharp drop ending near 680 cm^{-1}, and the kink near 780 cm^{-1}.

If the approximate tetragonal symmetry of SBT held sway over its optical properties in the infrared, then $E \| a$ and $E \| b$ would be equivalent. If this were the case, then the $E \perp c$ crystal reflectivity shown in the lower panel of Fig. 2 would correspond to a pure polarization, derivable from a single set of optical constants (such as ϵ_1 and ϵ_2, the real and imaginary parts of the dielectric function). To test this, the crystal reflectivity has been compared to a theoretical fit in Fig. 3.

The theoretical curve shown in Fig. 3 is based on the factorized form of the dielectric function[21–23]

$$\varepsilon(\nu)=\varepsilon_1(\nu)-i\varepsilon_2(\nu)=\varepsilon_\infty\prod_n \frac{\nu_{\mathrm{LO}n}^2-\nu^2+i\gamma_{\mathrm{LO}n}\nu}{\nu_{\mathrm{TO}n}^2-\nu^2+i\gamma_{\mathrm{TO}n}\nu}. \quad (5)$$

The factorized form for $\varepsilon(\nu)$ is more suitable than the classical-oscillator form, for ionic crystals having strong infrared bands with large TO-LO splittings.[22–24] The best-fit parameters are given in the upper part of Table II. The overall fit is quite reasonable. The TO and LO frequencies obtained for the main band are 612 and 773 cm^{-1}, respectively.

TABLE II. TO and LO frequencies of strong infrared modes in SBT, from reflectivity measurements.

	TO ν (cm^{-1})	LO ν (cm^{-1})	γ_{TO} (cm^{-1})	γ_{LO} (cm^{-1})	$\Delta\varepsilon_1$
					$\varepsilon_1(\infty)=5.5$
$E \perp c$	612	773	24	39	3.3
	333	451	16	57	7.3
	(230)	330	(58)	14	(17.0)
$E \| c$	780	815			
	(610)	675			
	(520)	(560)			

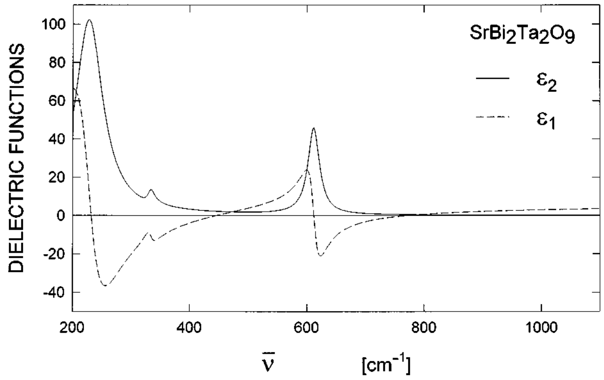

FIG. 4. Dielectric dispersion for $E \perp c$, obtained from the factorized-form fit to the crystal reflectivity.

The TO-LO pair at 333 and 451 cm^{-1} is required to fit the sharp reflectivity dip and the following edge in the 300–500 cm^{-1} region. The sharp dip is indicative of a TO frequency that follows closely on the LO of a nearby lower-lying mode. (See, for example, the $E \perp c$ reflectivity of anatase TiO$_2$ in Ref. 24.) This circumstance is indeed supported by the numbers in Table II.

Since the reflectivity data is poor below 250 cm^{-1}, the lowest TO frequency in Table II (listed in parentheses) is not reliable; it is included only for completeness in specifying the fit. The low-frequency region will be addressed in Sec. VII in which our infrared transmission measurements are discussed.

In the high-frequency region of Fig. 3, it can be seen that the measured reflectivity shows a small dip (relative to the theoretical curve) near 675 cm^{-1}. We interpret this dip as arising from an $E \| c$ LO mode observed as a consequence of the 11° deviation from normal incidence. With unpolarized incident light and the c axis normal to the surface (our experimental geometry), it is known that off-normal incidence will produce a shallow dip in an $E \perp c$ high-reflectivity plateau at the position of an $E \| c$ LO mode.[24,25]

Support for this interpretation of the weak 675 cm^{-1} feature in the crystal reflectivity is provided by the well-defined 675 cm^{-1} reflectivity edge seen in the polycrystalline pellet (top panel of Fig. 2). Attributing this clear feature of the pellet spectrum to its $E \| c$ component is consistent with the assignment of the 675 cm^{-1} feature to a strong LO edge of the $E \| c$ spectrum. This assignment is included in the lower half of Table II. The other entries given for $E \| c$ are discussed in Sec. VII.

The reasonableness of the fit shown in Fig. 3 is evidence that, at least in the spectral region investigated, the optical anisotropy in the ab plane is not large. If the reflectivity spectra for $E \| a$ and $E \| b$ were very different, a single $\varepsilon(\nu)$ function would not be expected to give a good account of the observed (admixed) reflectivity. This approximate isotropy in the ab plane confirms the influence of the parent tetragonal symmetry described in Sec. III.

Figure 4 shows the dispersion function ε_1 and ε_2 corresponding to Eq. (5) and the $E \perp c$ parameters of Table II. The signature of the main TO-LO pair (612 and 773 cm^{-1}), prominent in the center of Fig. 4, has the usual oscillator features; the peak in ε_2 is at the TO frequency, the high-

TABLE III. Zone-center phonon frequencies (ν in cm^{-1}) in SBT.

Infrared TO modes	Transmission expts. ν	k	Reflectivity expts. ν	k
	141	2.1		
$E \perp c$	188	3.0		
$E \perp c$	335	1.0	333	0.8
$E \parallel c$	545	0.7	(520)	
$E \perp c, E \parallel c$	614	3.9	612	5.0
$E \parallel c$	787	0.2	780	

Raman modes	28	167 (s)	250	430	607
	58	181 (s)	324	460	812 (s)
	80	213 (s)	365	518	

frequency zero of ε_1 is at the LO frequency. For the TO-LO pair at 333 and 451 cm^{-1}, these features are somewhat modified by damping and by the circumstance that they ride on a strong contribution from the unreliable low-frequency oscillator. For both the 612 and 333 cm^{-1} TO modes, the peak extinction coefficients corresponding to Fig. 4 agree fairly well with those obtained by infrared transmission measurements on thin films (Sec. VII).

In Fig. 4, ε_1 is seen to attain large values at low frequencies. In fact, these values are not large enough to account for the static (or very low frequency) dielectric constant of SBT; reported values of $\varepsilon_1(\nu \approx 0)$ lie in the range from 150 to 300.[2,3,9] The last column of Table II lists the contribution of each mode to $\varepsilon_1(0)$; the incremental increase in ε_1 on passing through each absorption band from high frequency to low, determined by successive applications of the Lyddane-Sachs-Teller (LST) relation.[21] The total yields an $\varepsilon_1(0)$ of 33. Low-frequency modes contribute much more than high-frequency ones (via the ν_{TO}^2 in the LST denominator), and the lowest-frequency contribution in Table II is incorrect because, as will be seen in Sec. VII, this TO frequency (230 cm^{-1}) in Table II is way off (too high). Correcting this doubles $\varepsilon_1(0)$ to 66, much closer to the observed values but still significantly too low. This means that we are missing some low-frequency infrared modes.

VI. EFFECTIVE CHARGES AND ION MOTIONS

The atomic masses (in amu) in SBT are: Sr, 88; Bi, 209; Ta, 181; O, 16. Since oxygen is so much lighter than the others, the high-frequency modes should be dominated by the motion of the oxygens. We expect this to be true of the high-frequency TO-LO pair at 612 and 773 cm^{-1}.

The complexity of the SBT primitive cell makes it difficult to calculate eigenvectors and eigenfrequencies from realistic models. But in ionic crystals, it is not unusual for the strongest infrared mode to be well approximated by a *rigid-sublattice* mode in which all positive-ion displacements are equal, all negative-ion displacements are equal (and in the opposite direction), and the ratio of the two displacements is determined by the masses (the center of mass is stationary).[26] In this section, we assume that the TO mode at 612 cm^{-1} corresponds to such a rigid-sublattice mode. Based on this assumed form for the vibrational eigenvector, we can then use the measured TO-LO splitting to estimate effective charges on the ions.

The masses yield a value of -0.166 for x_+/x_-, the ratio of the displacements of the positive (Sr, Bi, Ta) and negative (O) ions. The oxygens carry 86% of the kinetic energy, consistent with the identification with the high-frequency infrared mode.

Using the approach of Kurosawa[21] and assigning rigid-ion static charges to the ions (these charges are assumed to move with the ions), we obtain

$$(\omega_{\mathrm{LO}}^2 - \omega_{\mathrm{TO}}^2)\varepsilon_1(\infty) = 4\pi V^{-1}\left(\sum e_i^* x_i\right)^2 \left(\sum m_i x_i^2\right)^{-1}. \tag{6}$$

Here ω_{TO} and ω_{LO} are the angular frequencies of the high-frequency TO and LO modes, V is the primitive-cell volume, x_i is the displacement of ion i, e_i^* is the ion's charge, and m_i is its mass. The quantities on the left side of Eq. (6) are determined by our experiments (the entries in the top rows of Table III). On the right side, the x_i's are set by the x_+/x_- ratio. Charge neutrality and the assumption that all the oxygens have the same charge e_{O}^* then leaves e_{O}^* as the only unknown in Eq. (6). The result for e_{O}^* is $-3.8e$, where e is the magnitude of the electron charge.

Szigeti's introduction of the local-field correction[27] in the case of a cubic crystal reduces e^* by the factor $3/(\varepsilon_\infty + 2)$. SBT is not cubic, but our results indicate that the optical anisotropy is small in the ab plane. Our reflectivity-fit estimate for ε_∞ (Table III) is consistent with the value of the near-infrared refractive index of SBT.[28] Using ε_∞ to estimate the Szigeti effective charge for the oxygen ions yields a value of $-1.5e$. This is reasonable for nominally O^{--} ions.

Several assumptions are contained in the picture presented for the main infrared mode at 612 cm^{-1}, but the rigid-sublattice picture holds together fairly well. One assumption that is not realistic, but is easy to remedy, concerns the motions of the positive ions. Thus far, ''sublattice'' has been interpreted in a naive way for maximal simplification: the nine oxygen ions form one sublattice, the five positive ions form the other sublattice. Since their masses (and charges) are not all the same, it is unreasonable to lump the positive ions together in one rigidly translating sublattice. A more realistic treatment is to consider three positive-ion sublattices, with the strontiums, the bismuths, and the tantalums each having different (but parallel) displacements that are inversely proportional to their ion masses. Carrying out this program and taking the e_i^*'s to have their nominal ratios (+2/+3/+5/−2 for Sr/Bi/Ta/O) changes the Szigeti e_O^* by less than 1%. This insensitivity to the details of the cation motions comes about because both sums appearing in Eq. (6) are dominated by the contribution of the large oxygen-ion displacements. Thus this refinement in the treatment of the rigid-sublattice modes does not affect the conclusion that the main infrared band ($\nu_\mathrm{TO}=612\ \mathrm{cm}^{-1}$; $\nu_\mathrm{LO}=773\ \mathrm{cm}^{-1}$) corresponds approximately to a rigid-sublattice eigenvector dominated by oxygen-ion motion.

VII. INVENTORY OF INFRARED AND RAMAN FREQUENCIES

Thus far, the emphasis has been on the $E\perp c$ infrared eigenfrequencies derived from the crystal reflectivity. In Sec. V, an $E\parallel c$ LO-mode frequency was also identified (at $675\ \mathrm{cm}^{-1}$) with the help of the polycrystal (pellet) reflectivity. In this section, we see what more can be learned from the pellet reflectivity, present the results of infrared transmission measurements on SBT films, and—for completeness—include our Raman results.

Since the pellet reflectivity includes contribution from all three polarizations, while the crystal reflectivity determines the $E\perp c$ contribution, it might be supposed that the two spectra of Fig. 2 could be combined in a way to extract the $E\parallel c$ reflectivity spectrum. If the pellet reflectivity equaled $(\frac{2}{3})R(E\perp c)+(\frac{1}{3})R(E\parallel c)$, then $R(E\parallel c)$ would be given by $[3R_\mathrm{pellet}-2R_\mathrm{crystal}]$. Unfortunately, surface roughness appreciably distorts the reflectivity of a ceramic pressed pellet, depressing the measured reflectivity (relative to the true reflectivity of a dense polycrystalline material with an abrupt sample/air interface) at larger frequencies.[29,30] Thus $[3R_\mathrm{pellet}-2R_\mathrm{crystal}]$ is not available as a quantitative measure of the $E\parallel c$ reflectivity spectrum.

Nevertheless, since R_pellet exhibits features absent in R_crystal (and vice versa), it is possible to obtain some qualitative or semiquantitative information based on the location and shape of these features. In Fig. 2, features that are present in R_pellet but not in R_crystal are the steep drop near $675\ \mathrm{cm}^{-1}$ (already discussed), the band near $540\ \mathrm{cm}^{-1}$, and a small but definite band near $800\ \mathrm{cm}^{-1}$. (These features are even more pronounced in a plot of $[3R_\mathrm{pellet}-2R_\mathrm{crystal}]$.) For an isolated, well-defined, reststrahlen band, ν_TO occurs near the leading shoulder of the reflectivity plateau while ν_LO occurs near the trailing foot (compare the $612/773\ \mathrm{cm}^{-1}$ TO/LO frequencies with the main band in R_crystal). Using this as a guide to estimate TO and LO frequencies yields the values listed for $E\parallel c$ in the lower part of Table III. (Numbers in parentheses are rough estimates, less well pinned down than the others.) The TO values can be checked against the results of the transmission measurements to be discussed next.

Figures 5 and 6 present the results of infrared transmission measurements carried out on SBT films (0.25 μm in thickness) synthesized by a metalorganic solution-deposition technique.[9] Figure 5 shows results over the range from 300 to $2000\ \mathrm{cm}^{-1}$; Figure 6 shows results over the far-infrared range from 90 to $390\ \mathrm{cm}^{-1}$. Figure 6 includes results for six

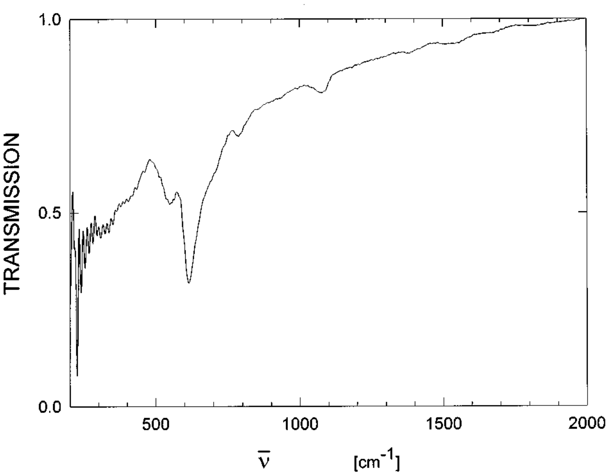

FIG. 5. Infrared transmission of an SBT thin film on a silicon substrate. The film was prepared by the solution-deposition technique described in Ref. 9 and annealed in air for 30 min at 650 C.

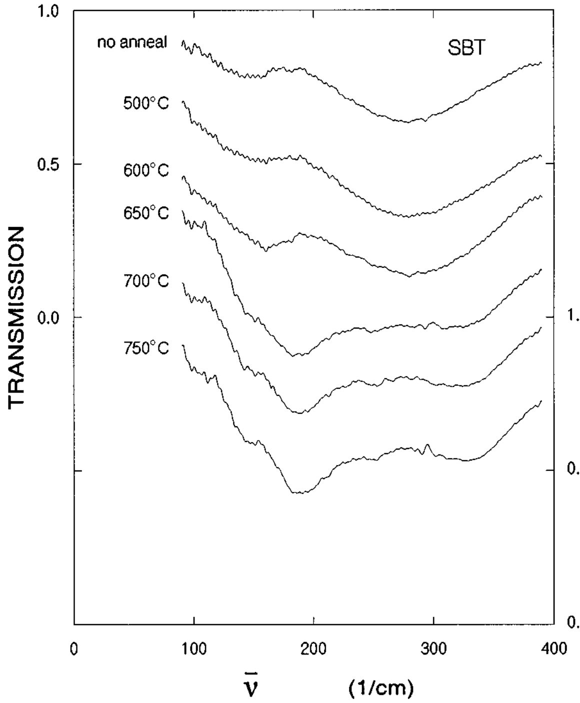

FIG. 6. Far-infrared transmission of SBT films prepared as in Ref. 9. Measurements were made at room temperature; each curve is labeled by the anneal temperature used in the film preparation. These curves have been smoothed to suppress interference fringes arising from the silicon substrates, using a smoothing function with a width of $4\ \mathrm{cm}^{-1}$. (Fringes are still discernible in the smoothed spectra; the fringe spacing is $4.5\ \mathrm{cm}^{-1}$.) This had no effect on the shape of the absorption bands, whose widths (full width at half maximum) are about $30\ \mathrm{cm}^{-1}$. For clarity, the curves have been vertically shifted from each other in steps of 0.2. The scale at the upper left applies to the top curve; the scale at the lower right applies to the bottom curve.

samples with different annealing histories. X-ray diffraction[9] shows that the films annealed at 650 C and above are composed of well-crystallized SBT with grain size of order 100 nm, while at lower anneal temperatures the films are amorphous. Figure 6 shows that the amorphous-to-crystalline transformation can be observed in infrared transmission via the appearance of characteristic absorption bands (notably the band at 188 cm^{-1}). In the range covered by Fig. 5, the strong band at 614 cm^{-1} provides a clear signature of crystalline SBT.[31] The broadness of the observed bands may be due to the nanocrystallinity of the films.

The SBT films of Figs. 5 and 6 were supported on silicon substrates 0.33 mm in thickness. Crystalline silicon, at this thickness, is transparent over the range shown. However, the annealing process (done in air) used to crystallize the SBT produces an oxide film on the substrate. It is this silicon oxide film that gives rise to the high-frequency absorption band appearing in Fig. 5 at 1072 cm^{-1}. The position and strength of this band indicates that the film is a 15 nm layer of amorphous $\mathrm{SiO}_{1.8}$.[32] The other bands seen in Figs. 5 and 6 are assigned to SBT.

The positions and strengths of the SBT absorption bands observed in thin-film transmission are listed in Table III. The positions correspond to TO frequencies, and reflectivity-derived TO frequencies are included in this table. The reflectivity-derived TO at 612 cm^{-1} for the main $E\perp c$ reststrahlen band agrees well with the strongest absorption line at 614 cm^{-1}. In Table III, oscillator strength is expressed in terms of k, the peak value of the dimensionless extinction coefficient (related to the optical absorption coefficient α by $\alpha=2\omega k/c$). For the transmission measurements, k was obtained from α via $\alpha d=\ln(t_0/t)$, where d is the film thickness, t is the transmission minimum of the band, and t_0 is the background transmission in the neighborhood of the band. For the $E\perp c$ TO frequencies at 612 and 333 cm^{-1} obtained by fitting the crystal reflectivity, k was determined from the dielectric functions of Fig. 4. These k values are in reasonable agreement with the corresponding k's estimated from thin-film transmission.

Six infrared TO frequencies are collected in Table III. The two values derived from the $E\perp c$ crystal reflectivity agree very well with their transmission-derived counterparts. For the others, the transmission-derived values are expected to be more accurate. The TO roughly estimated for $E\| c$ from reflectivity (the 610 cm^{-1} entry in Table II) is not separately listed in Table III, but is included with the 614 cm^{-1} transmission-derived entry. The (230) entry of Table II is dropped in Table III, since no line near 230 cm^{-1} was observed in transmission. The closest line seen in transmission is at 188 cm^{-1}. If we assume that 188 cm^{-1} is the correct TO frequency belonging in the last line of the $E\perp c$ portion of Table II (paired with the LO at 330 cm^{-1}), this substantially increases the TO-LO splitting and thereby increases this band's dielectric-constant contribution from 17 to 50 and increases the calculated static dielectric constant to 66. This large value is still appreciably smaller than experimental estimates, and this deficit in $\varepsilon_1(0)$ means that we are missing the contribution of low-frequency infrared modes occurring below our experimental limit of about 90 cm^{-1}.

The LO frequencies corresponding to the TO's of Table III are contained in Table II. As discussed above, the 188 cm^{-1} TO mode is taken to be the TO counterpart of the $E\perp c$ 330 cm^{-1} LO mode. The LO counterpart of the 141 cm^{-1} TO frequency is unknown. For the $E\perp c$ 612 cm^{-1} TO mode, the corresponding LO mode is at 773 cm^{-1}. For the $E\| c$ TO mode at nearly the same TO frequency, the corresponding LO frequency is about 675 cm^{-1}.

The six TO frequencies of Table III correspond to ten or eleven vibrational modes. To see this, we invoke the *ab*-plane optical isotropy implied by the $E\perp c$ reflectivity to support the claim that each of the three observed $E\perp c$ reststrahlen bands corresponds to two modes, one active for $E\| a$ and the other active for $E\| b$. Each $E\perp c$ frequency in Table III thus represents two modes. Each $E\| c$ frequency represents one mode. The polarization of the 141 cm^{-1} band is not known. The arithmetic then yields ten or eleven, depending on the polarization of the 141 cm^{-1} band.

The bottom part of Table III contains our Raman results for SBT. Fourteen Raman lines are listed, based on our measurements on both pellets and crystals. Graves *et al.*[8] observed the nine lines above 200 cm^{-1}, but their stated frequencies are evidently consistently low by about 12 cm^{-1}.

The number of Raman lines we observed (14) can be compared to the numbers given in Table I: 12 are permitted for the tetragonal structure, 81 for the orthorhombic. There is a further complication not discussed earlier: For the orthorhombic structure, the complexity is even worse than it seems from Table I. This is because, for orthorhombic SBT, 61 of the 81 Raman modes are also infrared-active [Eq. (2)] giving rise to TO-LO pairs. Since these LO modes are also Raman allowed, the actual number of possible Raman lines is 142. While the number we observe is much smaller than this, it does exceed the number possible for the tetragonal structure. This is of course consistent with the actual orthorhombic structure.

The preceding paragraph reveals that most of the Raman frequencies observed for SBT should correspond to TO or LO infrared frequencies. However, examination of the numbers in Tables II and III finds only two candidates for this among the Raman lines (607 and 812 cm^{-1}). While part of the reason for this absence of coincidence must be that only a fraction of the IR and Raman lines have been observed, it is likely that there is also another reason: the smallness of the distortion from the tetragonal structure. Since the tetragonal structure has a center of symmetry, there is mutual exclusion between Raman and infrared activity. This property no longer holds with the introduction of the orthorhombic distortion, but a residual effect of near-centrosymmetricity can remain, namely a strong inverse correlation between Raman and infrared intensity. Such ''complementarity'' (modes strong in Raman are weak in infrared, modes weak in Raman are strong in infrared) occurs for cinnabar structure HgS,[26] which is a simpler example of a low-symmetry structure that can be treated as a distortion of a centrosymmetric structure. Since only the strongest infrared modes of SBT are reported here, complementarity makes it unlikely that the Raman lines seen at 607 and 812 cm^{-1} arise from the similar-frequency TO and LO modes found in Tables II and III.

Comparisons to some simpler oxides can be made, as is sometimes attempted for phonons in the similarly complex bismuth-based cuprate superconductors.[33] $\mathrm{Bi_2O_3}$ presents a dense spectrum of infrared and Raman lines from 540 cm^{-1}

downward, including infrared bands[33] at 38 and 58 cm^{-1} (below our infrared range of measurement) and Raman bands[34] near 60 cm^{-1}. It is likely that bismuth displacements play a major role in the eigenvectors corresponding to the two low-frequency Raman lines listed in Table III. SrO has the rocksalt structure; its TO and LO frequencies occur at 230 and 480 cm^{-1}.[35] Ta_2O_5 has a prominent infrared band at 624 cm^{-1},[36] a frequency close to that of the 613 cm^{-1} TO mode discussed in Sec. VI.

More work needs to be done. It would be valuable to extend investigation to the region below 100 cm^{-1}. Significant low-frequency infrared-active modes are missing from our collection; this is shown by the dielectric-constant deficit discussed at the end of Sec. V. Also, this region should exhibit modes connected to the ferroelectricity of SBT. These studies may require the availability of large single crystals.

VIII. SUMMARY

A group-theoretical analysis of the 28-atom primitive cell of orthorhombic SBT was carried out, yielding the phonon-symmetry results of Eq. (2) and, in Table I, a comparison with the infrared and Raman expectations for the parent tetragonal structure. From reflectivity (Figs. 2 and 3) and thin-film transmission (Figs. 5 and 6) measurements, we have determined the frequencies of the main infrared-active phonons in SBT (Table III). The reflectivity observed for $E\perp c$ was well fit by a factorized-form dielectric function in the region above 300 cm^{-1}, where the influence of the approximate tetragonal symmetry imposes a near-isotropy in the ab plane. The prominent high-frequency band, with TO and LO frequencies at 613 and 773 cm^{-1}, arises from a mode dominated by the motion of the oxygen sublattice. The oxygen-ion Szigeti effective charge is estimated to be $-1.5e$. Frequency estimates for the TO (LO) pairs of other strong bands are 188(330) and 334(451) cm^{-1} for $E\perp c$, and 610(675) and 780(815) cm^{-1} for $E\parallel c$. In addition to the main infrared bands, the main Raman bands of SBT are also reported.

ACKNOWLEDGMENTS

It is a pleasure to thank Gerry Gibbs for clarifying discussions about the space-group symmetries of SBT and for making available his Xtalpow software. We are indebted to Wantana Songprakob and Sathon Vijarnwannaluk for some of the transmission measurements and to Xubai Zhang for providing the pressed pellet. We have also benefitted from the help of Cindy Davis, John G. Thompson, and Dilip Vijay.

---

*Present address: Volvo Aero Corporation, Materials R&D, Trollhattan, Sweden.

[1] B. Aurivillius, Arkiv for Kemi **1**, 463 (1949).

[2] G. A. Smolenskii and A. I. Agranovskaya, Sov. Phys. Solid State **1**, 400 (1959); G. A. Smolenskii, V. A. Isupov, and A. I. Agranovskaya, *ibid.* **3**, 651 (1961).

[3] E. C. Subbarao, J. Phys. Chem. Solids **23**, 665 (1962).

[4] J. F. Scott, Phys. World 1995, 46; J. F. Scott, F. M. Ross, C. A. Paz de Araujo, and M. Huffman, MRS Bull. **21**, 33 (1996).

[5] C. A. P. Araujo, J. D. Cuchiaro, L. D. McMillian, M. C. Scott, and J. C. Scott, Nature (London) **374**, 627 (1995).

[6] R. E. Newnham, R. W. Wolfe, R. S. Horsey, F. A. Diaz-Colon, and M. I. Kay, Mater. Res. Bull. **8**, 1183 (1973). The crystals used in this study had 10% of the Sr atoms replaced by Ba.

[7] A. D. Rae, J. G. Thompson, and R. L. Withers, Acta Crystallogr., Sect. B: Struct. Sci. **48**, 418 (1992).

[8] P. R. Graves, G. Hua, S. Myhra, and J. G. Thompson, J. Solid State Chem. **114**, 112 (1995).

[9] P. C. Joshi, S. O. Ryu, X. Zhang, and S. B. Desu, Appl. Phys. Lett. **70**, 1080 (1997).

[10] S. B. Desu, D. P. Vijay, X. Zhang, and B. P. He, Appl. Phys. Lett. **69**, 1719 (1996).

[11] H. G. von Schnering *et al.*, Angew. Chem. **27**, 574 (1988); M. Cardona *et al.*, Solid State Commun. **66**, 1225 (1988). $Bi_2Sr_2CaCu_2O_8$ consists of alternating Bi_2O_2 and $Sr_2CaCu_2O_6$ layers. Like SBT it is orthorhombic, slightly distorted from $I4/mmm$ tetragonal, with two primitive cells per orthorhombic unit cell and two formula units per primitive cell. The CuO_2 planes have the same square-lattice geometry as the TaO_2 planes in SBT. But unlike the tantalums in SBT, the coppers in BSCCO (a.k.a. Bi2212) are pyramidal (CuO_5), not octahedral, because the interplane bridging oxygen is missing.

[12] E. C. Subbarao, J. Am. Ceram. Soc. **45**, 166 (1962), Fig. 1(A); J. Robertson, C. W. Chen, W. L. Warren, and C. D. Gutleben, Appl. Phys. Lett. **69**, 1704 (1996), Fig. 1; also see Fig. 1 of Ref. 2 (1961), and Fig. 1(a) of Ref. 5.

[13] Figure 3 of Ref. 1.

[14] *International Tables for Crystallography, Volume A, Space-Group Symmetry*, edited by T. Hahn (Kluwer, Dordrecht, 1989), pp. 468–469.

[15] In Wyckoff notation, the strontiums and perovskite-midplane oxygens occupy a and b sites of $I4/mmm$, the bismuths occupy e sites, the tantalums occupy another set of e sites, the oxygens in the Bi_2O_2 midplane occupy d sites, the perovskite-slab outer oxygens (not corner sharing) occupy e sites, and the other four-ninths of the oxygens (in the Ta planes) occupy g sites.

[16] Ref. 4, pp. 230–231.

[17] In Wyckoff notation, the strontiums and perovskite-midplane oxygens occupy sites of $A2_1am$, all the other atoms occupy b sites.

[18] The characters of Γ are conveniently obtained from the vector (x,y,z) representation and the site-permutation characters $s(\alpha)$, as described by R. Zallen, R. M. Martin, and V. Natoli, Phys. Rev. B **49**, 7032 (1994). For orthorhombic SBT, $s(1)=28$, $s(2_a)=s(2_b)=0$, and $s(2_c)=4$. The last corresponds to the four perovskite-midplane atoms, which lie on the mirror plane.

[19] Ref. 8. In the terminology used by these authors, symmetrized corrdinates are referred to as ‘‘modes’’ or ‘‘normal vibrational modes.’’ But these are not the actual vibrational-mode eigenvectors. The true normal-mode eigenvectors are as-yet-undetermined linear combinations of same-symmetry symmetrized coordinates. Only for simple high-symmetry crystals can vibrational-mode eigenvectors be determined by symmetry alone. An oxide example is the anatase form of TiO_2, in which the lone A_{2u} optical mode is symmetry determined but the two E_u optical modes are not [R. J. Gonzalez *et al.*, Phys. Rev. B **55**, 7014 (1997)]. Reference 8 is concerned with Raman-active modes, and the results stated there for the number and symmetry

types of the Raman modes of tetragonal SBT (in their discussion, SBT is an Aurivillius phase of order $n=2$) are correct. However, Ref. 8 overcounts the number of infrared modes, because the acoustic (zero-frequency) modes are included and because the silent B_{2u} mode is listed as infrared active.

[20] The software used to generate the powder pattern from the atomic positions and the space group is called Xtalpow and was developed at Virginia Tech by G. V. Gibbs and his colleagues. A description is given in R. J. Downs, K. L. Bartelmehs, G. V. Gibbs, and M. B. Boisen, Am. Mineral. **78**, 1104 (1993). The atomic positions were taken from Ref. 6.

[21] T. Kurosawa, J. Phys. Soc. Jpn. **16**, 1298 (1961). Setting $\nu=0$ in the factorized form yields the Lyddane-Sachs-Teller relation.

[22] D. W. Berreman and F. C. Unterwald, Phys. Rev. **174**, 791 (1968).

[23] F. Gervais and B. Piriou, Phys. Rev. B **10**, 1642 (1974); J. F. Baumard and F. Gervais, *ibid.* **15**, 2316 (1977).

[24] R. J. Gonzalez, R. Zallen, and H. Berger, Phys. Rev. B **55**, 7014 (1997).

[25] A. S. Barker and M. Ilegems, Phys. Rev. B **7**, 743 (1973).

[26] R. Zallen, G. Lucovsky, W. Taylor, A. Pinczuk, and E. Burstein, Phys. Rev. B **1**, 4058 (1970).

[27] B. Szigeti, Trans. Faraday Soc. **45**, 155 (1949).

[28] T. C. Chen, Ph.D. dissertation Virginia Tech, 1995. The refractive index measured at $\nu=10^4$ cm^{-1} is 2.38, corresponding to $\varepsilon=5.66$.

[29] V. Hopfe, E. H. Korte, P. Klobes, and W. Grahlert, Appl. Spectrosc. **47**, 423 (1993).

[30] M. P. Moret, MS thesis, Virginia Tech, 1996, p. 92.

[31] M. P. Moret and R. Zallen (unpublished).

[32] H. R. Philipp, in *Handbook of Optical Constants of Solids*, edited by E. D. Palik (Academic, New York, 1985), pp. 762 and 769.

[33] Z. V. Popovic, C. Thomsen, M. Cardona, R. Liu, G. Stanisic, R. Kremer, and W. Konig, Solid State Commun. **66**, 965 (1988).

[34] S. N. Narang, N. D. Patel, and V. B. Kartha, J. Mol. Struct. **327**, 221 (1994).

[35] K. H. Rieder, R. Migoni, and B. Renker, Phys. Rev. B **12**, 3374 (1975).

[36] U. Balachandran and N. G. Eror, J. Mater. Sci. Lett. **1**, 219 (1982).